Hindawi
Advances in Civil Engineering
Volume 2024, Article ID 1008274, 16 pages
https://doi.org/10.1155/2024/1008274

Research Article

Response and Damage Characteristics of Segmental Tunnel Lining under Various Dynamic Load Conditions

Jinling Chai, Ke Wang, Shihao Wang, Yong Wang, and Yi Liu

Department of Architectural Engineering, Henan College of Transportation, Zhengzhou 450000, China

Correspondence should be addressed to Shihao Wang; wang.shihao99@outlook.com

Received 8 December 2023; Revised 22 March 2024; Accepted 6 April 2024; Published 17 April 2024

Academic Editor: Chu Zhaofei

This paper investigates segmental lining, developing a numerical model to explore the dynamic interaction between saturated soil and the lining structure, and analyses the effects of the angle of incident load and the wavelength-to-diameter ratio on the displacement, deformation, and distribution of the plastic zone of the structure. The findings demonstrate that the structure experiences vertical compressive deformation during ground shock predominantly. The structure can be categorised into the major deformation region (with an angle within 60° of the vertical direction) and the minor deformation region (with an angle within 30° of the horizontal direction), determined by the structure's radial deformation. The maximum radial velocity of the nodes in the major deformation area is greater and swifter, whereas the maximum radial velocity of the nodes in the minor deformation region is lesser and mostly equivalent in extent. The maximum radial displacement of the nodes in the major deformation area is highly receptive to the loading wavelength–diameter ratio (L/D) (the ratio of the load wavelength to the structure's outer diameter) when the wavelength-to-diameter ratio (L/D) is small ($1 \le L/D \le 5$). Conversely, the maximum radial displacement in the minor deformation area is considerably sensitive to the wavelength–diameter ratio when $5 \le L/D \le 30$. The total displacement and velocity of the structure remain unaffected by the angle of load incidence. However, it affects the maximum deformation of the structure as well as the location where the maximum node velocity occurs. In addition, the joint surface of the structure experiences the highest plastic strain at an angle of load incidence of 60°.

1. Introduction

With the continuous development of urban underground transport systems, the safety of underground structures is related to the normal operation of the entire city, especially for the underground and other densely populated places, and the difficulty of evacuating and rescuing people in the event of an attack, coupled with the seriousness of the secondary disaster, has a great potential for damage to the structure, life, and the environment. More importantly, for shield tunnels in saturated soils, if a large deformation of the structure occurs and a hole is formed, a large amount of silt will then pour into the interior of the tunnel, causing secondary damage and triggering an even greater disaster. It has been reported that in the underground structure in New York City across the Hudson River section due to the long time of construction, a small explosion may cause perforation; if the river water enters into the tunnel, the consequences will be catastrophic [1, 2], and many cities, such as London, Paris, Tokyo, and Singapore, in the world underground lines contain sections across the river and many cities in the south of China. The top of the underground tunnels is buried in shallow depths [3, 4], which are more dangerous when subjected to external impact loads, such as the Shanghai Chongming Crossing river tunnel at an average depth of 9 m, and the shallowest depth is only 6.8 m [5]. In shield tunnels, prefabricated concrete segments are mostly used for lining, and a circular cross-section is the most common. Therefore, the object of this paper is set as the lining structure of shield tunnels with a circular cross-section, and the geometric dimensions of the structure and the materials used are based on the lining structure of the shield tunnel in a certain city. The guidelines given by the International Tunnelling Association (ITA) on the design of segmental lining structures for shield tunnels take into account the incidental loads or effects caused by the corresponding natural disasters and some man-made factors, such as earthquakes,

wind loads, fires, etc., but do not take into account the effects of ground shock [6]. Therefore, in the context of researching blast resistance, it is essential to urgently investigate the mechanical response and damage characteristics of shield tunnel lining structures including displacement, deformation distribution, and mechanical properties of joints, caused by ground shock such as nuclear explosions.

For the research method of mechanical response of segmental lining structure under external explosion load, the current research results mainly focus on numerical simulation and simplified theoretical analysis. Koneshwaran et al. [7] assessed the resilience of buried tunnels to surface explosions using ALE and SPH techniques, finding ALE to be more efficient and accurate, and reveals that different segmented bored tunnel designs exhibit varied responses to blasts, with modern ring-type tunnels showing flexibility but suffering from permanent drifts, indicating the need for careful consideration in their implementation in civil engineering. Yang et al. [8] use ANSYS/LS-DYNA to study the dynamic response of the tunnel lining structure in the case of an explosion of different equivalents of TNT in a shallow underground tunnel. De et al. [9] compared the explosion test data under 70 g acceleration with the numerical simulation results, and the results showed that the strains of the tunnel lining structure were correlated with the depth of overburden and the depth of water. Rashiddel et al. [10] demonstrated that segmental tunnel linings with curved joints exhibit superior efficiency and stability under surface explosion loads compared to planar segmental and continuous linings, achieving lower bending moments, axial forces, and deformation amounts in response to blast stress. Zhang et al. [11] revealed that the dynamic response of tunnel linings is significantly influenced by the horizontal and vertical distances between adjacent tunnels, with increased height differences leading to higher vibration velocities and displacements due to more effective stress wave reflection and superposition. Xiong et al. [12] investigated the impact of blasting pressure on subway tunnel lining stability, establishing a safe blasting distance to ensure the structural safety of adjacent subway tunnels, validated through field data comparison and analysis of PPV, frequency, and Von Mises stress distribution.

Wang et al. [13] utilised the saturated porous medium heat-fluid-heat-flow-induction (HFHI) method. The dynamic response of a tunnel structure in saturated soft clay under exponentially attenuating impact load is investigated using a coupled thermal-fluid-solid dynamic response model for porous media. Wang et al. [14] assumed the tunnel lining segments to be rigid, and the tensile, compression, shear, and bending properties of the joints are considered. A simplified calculation method for the dynamic response of the structure under the ground shock is proposed, and the influence of the wavelength–diameter ratio is studied.

The current study entails the development of a 3D finite element model of the prototype lining structure in fully saturated soil. To achieve this, we based our research on the propagation law of shock wave in nonuniform partially saturated soil in [15] and the boundary condition setting in the finite element software calculation in [16]. We also examine the interaction between the lining structure and saturated soil and further discuss the structural displacements, deformations, node velocities, and the distribution law of plastic zones in varying working conditions. Our objective is to investigate the damage characteristics of segmental lining under the action of the ground shock.

2. Numerical Model

2.1. Model Boundary Condition Setting. The soil in this paper's numerical model is modeled using the P-α numerical model validated with [14]. The air content in the model was set to zero to compute the stress–strain relationship and imported into the computational model. To reduce the number of cells in the saturated soil model and enhance calculation speed, the lateral vertical boundaries of the model were established using the dynamic artificial boundaries outlined in [16]. Figure 1 shows that the application process is divided into the following two steps:

(1) Establish a saturated soil model consisting of a single column of solid elements with symmetric lateral boundaries, and the direction of ground motion load propagation is parallel to the lateral boundaries, calculate the propagation law in the ground motion load model, and record the stress–time curve of each element.

(2) A procedure is written to map the resulting unit stress time-range curves at different heights to the boundaries *Bb* and *Bd* of the numerical model of saturated soil at the corresponding heights according to [15], and the vertical boundaries of the numerical model of the prototypical structure's interaction with the saturated soil dynamics are set to be nonreflective boundaries.

As illustrated in Figure 1, we have set the load boundary *Ba* and the bottom boundary *Bc* of the model as nonreflective boundaries to avoid the reflected loads generated on the structure reflecting on the boundaries. Consequently, for the ground shock that are meant to be applied to the structure, the actual load $P(t)$ on the loading boundary must be twice the intended load [16]. The numerical model was established based on an underwater shield tunnel. The inner diameter of the lining is 5.5 m, the outer diameter is 6.2 m, and the width of the single-ring lining in the travelling direction is 1.2 m.

2.2. Constitutive Model and Contact Interactions. Considering the homogeneity of the ground impact load in the plane, a ring in the lining structure can be extracted separately, and the intercepted cross-section is processed according to the symmetry plane, so that the number of elements can be effectively reduced and the speed of calculation can be improved without affecting the calculation results. The numerical model mainly includes the concrete part of the segments, the rebars, the ring bolts, and the surrounding saturated soil. The closest distance between the upper and lower boundaries, as well as the left and right boundaries, and the structure is 1.5 times the outer diameter of the structure, i.e., 9.3 m. The specific finite element model is shown in Figure 2, and the concrete model

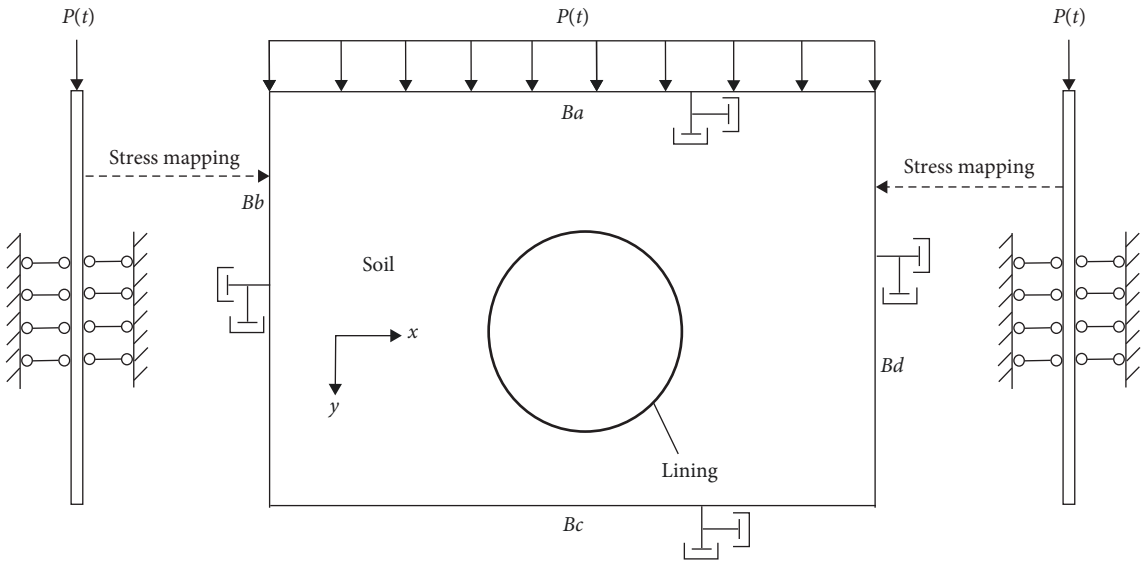

Figure 1: Schematic of numerical model boundary setting.

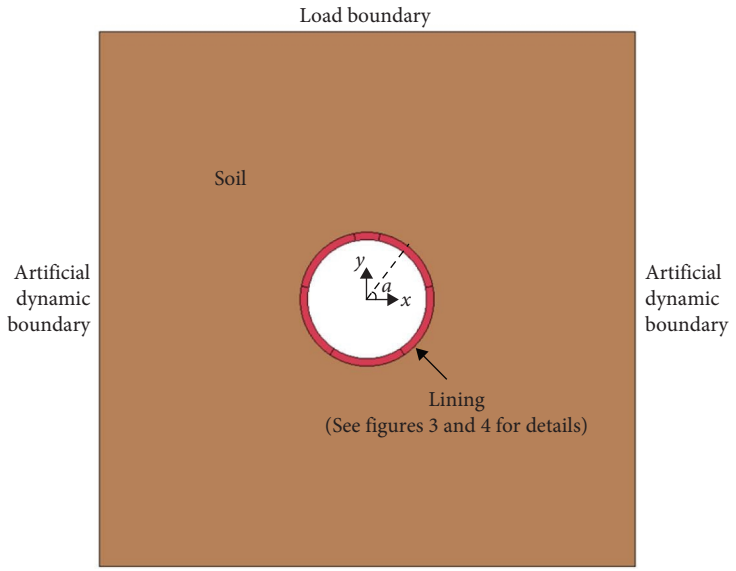

Figure 2: Finite element model.

of the lining, the distribution of the rebars, the distribution of the bolts, and the bolt detail are shown in Figure 3(a)–3(d), respectively.

In the numerical model of the lining, the rebars and the concrete segments are established separately, and the interaction between the rebar and concrete is simulated by CONSTRAINED_LARGRANGE_IN_SOLID. The interaction between the segments, bolts, and media is calculated using the AUTOMATIC_SINGLE_SURFACE algorithm, and the study of [17] shows that the contact algorithm can solve the contact problem in the model well.

The *MAT_WINFRITH_CONCRETE material model that considers the strain rate effect is used in the numerical model established in this paper to describe the concrete of the segments, and the development of the cracks in the segments under ground shock can be output by incrementing the $q =$ D3CRACK command. The pressure versus volumetric strain curves of the material model are shown in [18]. The material model multiplies the modulus of elasticity of concrete by a correction factor to describe the strain rate effect of concrete. The coefficient ranges from 1 to 2.2 when the strain rate of concrete in compression is between 0 and $50\,s^{-1}$ and increases linearly with increasing strain rate; the coefficient ranges from 1 to 2 when the strain rate of concrete in tension is between 3×10^{-5} and $50\,s^{-1}$ and increases linearly with increasing strain rate.

The rebars and bolts in the model are described by the *MAT_PLASTIC_KINEMATIC material, which can be adjusted by adjusting the hardening parameter β to adjust

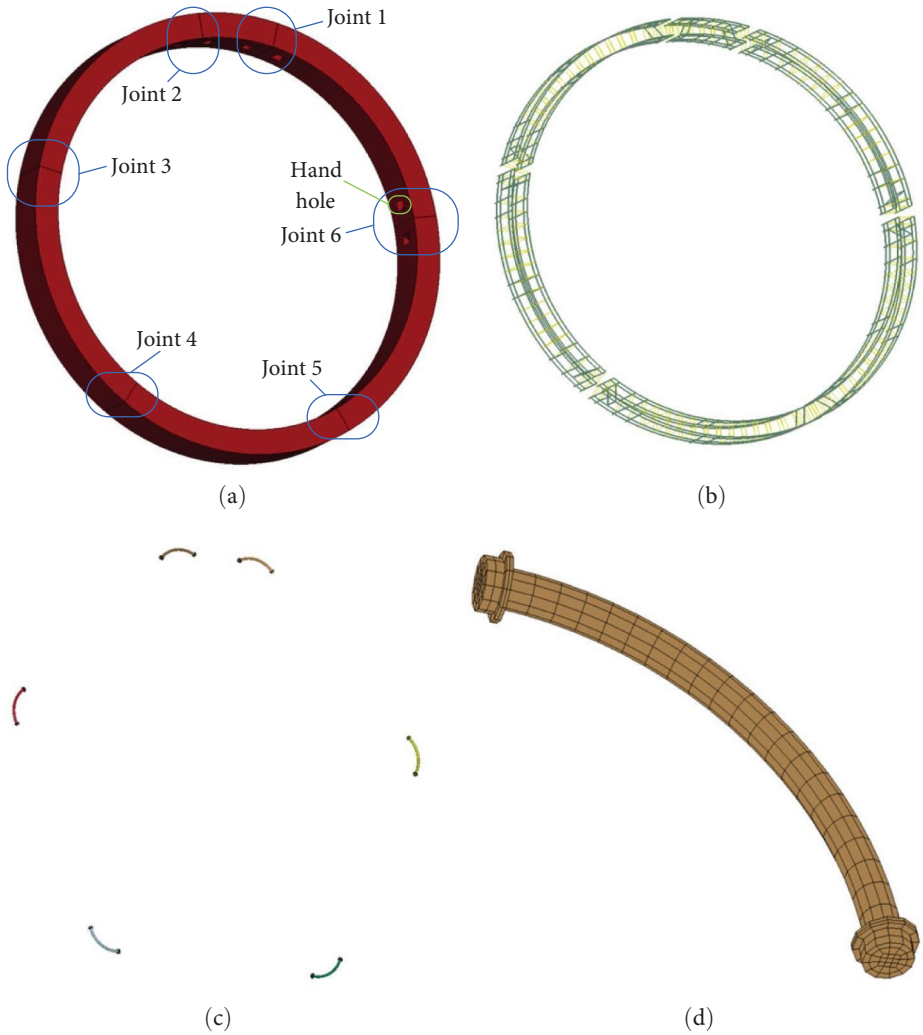

Figure 3: Segmental lining: (a) concrete segments, (b) rebars arrangement, (c) bolts arrangement, and (d) bolt details.

Table 1: Material parameters of rebars and bolts.

Material	Density (kg/m^3)	Elastic modulus (GPa)	Poisson's ratio	Compressive strength (MPa)	Tensile strength (MPa)
Rebar	7800	200	0.25	468.0	468.0
Bolt	7800	210	0.23	468.0	468.0
Concrete	2650	34.5	0.2	60	4.96

the proportion of isotropic reinforcement. In the numerical model of this paper, the hardening modulus of the rebar is approximated to be 0.01 times of the modulus of elasticity E, and the value of the hardening parameter β is set to be 1. The strain rate effect of the reinforcement and bolts can be adopted from the Cowper–Symonds model.

The specific material parameters of the rebars and bolts are shown in Table 1.

3. Results and Discussion

3.1. The Effects of Incidence Load Angle on Structural Response. In actual projects, the lining is often assembled with staggered joints along the length of the tunnel, so that the angle between the direction of the load and the center of the lining small segment is not 0, causing the mechanical response of the structure to be different from the previous results. The load acting on the structure from directly above the small segment is taken as the forward incident condition, and the structure is rotated counterclockwise by a certain angle, which is defined as the incident load angle ξ, the angle between the line connecting the center of the lining and the midpoint of the smallest segment and the vertical direction, to calculate the motion and dynamic response of the lining at different angles (0°, 30°, 60°, and 90°).

3.1.1. Lining Displacement and Deformation. Since there is basically no horizontal displacement of the top and bottom

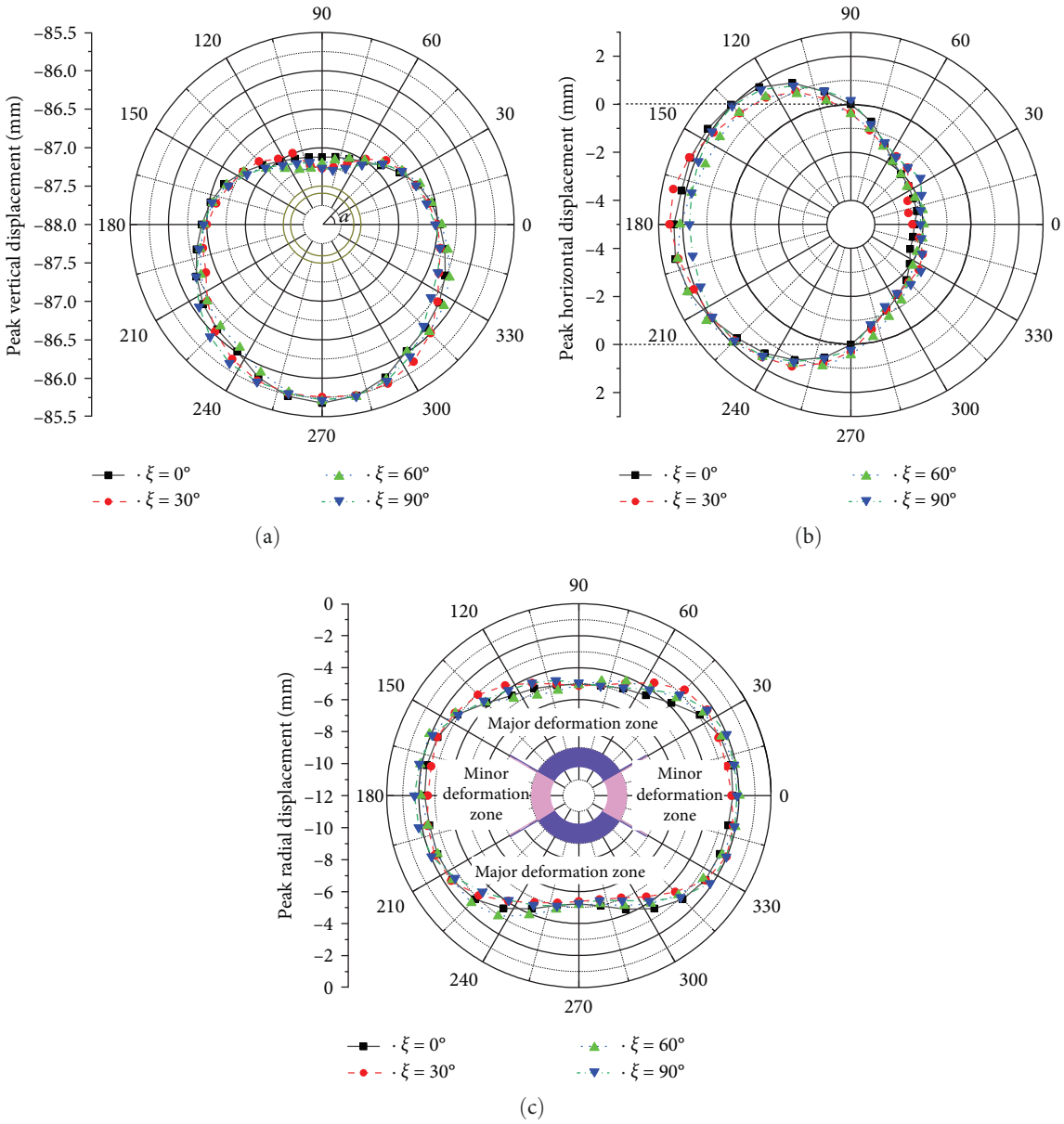

Figure 4: Peak displacement distribution with different incidence load angles: (a) peak vertical displacement, (b) peak horizontal displacement, and (c) peak radial displacement.

nodes of the structure during the whole response process of the structure, it can be considered that the structure mainly undergoes total vertical stiffness displacement and a certain degree of deformation, and the centre of the structure in the deformation process is defined as the midpoint of the connecting line of the nodes on both sides of the structure; the radial displacements of the nodes which describe the deformation of the structure can be calculated according to Formula (1):

$$u_{r,\alpha}(t) = \left(u_{y,\alpha}(t) - \frac{u_{y,\alpha=0}(t) + u_{y,\alpha=180}(t)}{2}\right)\sin\alpha + u_{x,\alpha}(t)\cos\alpha. \quad (1)$$

Figure 4 shows the distribution curves of the peak displacements in each direction of the structure under different incidence load angles. The change of the angle ξ basically does not change the distribution pattern of the peak displacements in each direction of the structure in the annular direction, and there are only some differences in the values of each node and the locations where the maximum values of the peak displacements appear. In Figures 4(a) and 4(b), when ξ is not zero, the vertical and horizontal displacement peak values near the top of the structure change significantly. When $\xi = 30°$ and 90°, it appears as small on the left and large on the right. When = 60°, the left side is larger and the

right side is smaller. In Figure 4(c), when $\xi = 30°$ and 90°, the peak radial displacement near the top of the structure is smaller on the left and larger on the right. The peak displacement near the bottom of the structure is basically axially symmetrically distributed, and both are greater than the peak displacement with $\xi = 0°$. When $\xi = 60°$, the peak radial displacement near the top of the structure is larger on the left and smaller on the right, and near the bottom of the structure, it is larger on the left and smaller on the right. In summary, the incidence load angle basically does not affect the displacements of the structure but changes the location where the maximum deformation of the structure occurs.

3.1.2. Lining Velocity Distribution. Figure 5 shows the distribution curves of the peak velocity in each direction of the structure with different incidence load angles. In Figure 5(a)–5(c), the change of the angle ξ basically does not change the distribution law of the peak velocity in each direction of the structure in the annular direction, and there are some differences only in the value of each node and the location where the maximum value of the peak velocity appears.

In Figure 5(c), the differences in the peak radial velocities of the structure under different conditions are mainly found at the top and bottom of the structure. The peak radial velocities of the nodes near the top of the structure are basically the same when $\xi = 0°$, but the peak velocities near the bottom of the structure are larger when $\xi = 30°$. The peak velocities at the bottom of the structure are larger when $\xi = 60°$ and 90° than the other conditions. In summary, the angle of load incidence basically does not affect the total motion velocity of the structure, but it does alter the location of maximum node velocity.

3.1.3. Lining Damage Characterisation. Figure 6(a)–6(d) shows the plastic strain distribution on the structure under the conditions of incidence load angles of 0°, 30°, 60°, and 90°, respectively, and it can be seen that the plastic strains on the structure mainly appeared around the joints, handholes, and joint surfaces. The results are in agreement with that of [19]. Due to the presence of right angles in the handhole area of the bolt at the joint of the segments in the numerical model, whereas the actual structure has undergone some arc treatment, the plastic strain near the handhole in the result may exceed that of the actual structure. The investigation of the structure's damage morphology under ground shock can be revealed by analysing the distribution of the plastic strain on the joint surface.

The deformation of the joint components depicted in Figure 6 can be classified into two main types. First, the plastic strain on the joint surface is concentrated towards the outer surface, extending to the inner surface, and resulting in radial penetration, for instance, joints 1 and 2 at both ends of the sealing ring when $\xi = 0°$. Second, joint 4 at $\xi = 30°$, and so on, is in a state of positive bending. The plastic strain on the joint surface is concentrated on the inner area and extends towards the outer surface. This is observed in joints like joint 6 when $\xi = 0°$, joints 1 and 2 when $\xi = 90°$, etc., which are in the negative bending state.

The maximum plastic strain on the joint surface under different conditions and the location of its occurrence are different, and the specific values are shown in Table 2. It can be found from Table 2 that the maximum plastic strain in the structure increases with the increase of ξ between $0° \le \xi \le 60°$ and decreases with the increase of ξ between $60° \le \xi \le 90°$, which indicates that the incidence load is the most unfavourable to the structure when the angle of incidence of load is 60°, and this is in line with the results of the study in [20].

3.2. The Effects of the Wavelength–Diameter Ratio. The peak and duration of a shock wave generated by a nuclear explosion with durations ranging from a minimum of a few tens of milliseconds to a maximum of a few seconds and the wavelength of the shock wave can be obtained by multiplying the velocity of the wave in the medium by the duration. When the structure is located in saturated soils described in [15], the wavelength varies from tens to hundreds of metres. When the source of the burst is located at the surface, the wavelength is smaller because shield tunnels within cities generally have smaller burial depths and shorter durations of ground shock on the lining structure [21]. Li and Li [22] analysed the dynamic response of unlined circular cavern under triangular loading and found that the wavelength–diameter ratio L/D has a great influence on the maximum node displacement and velocity of the lining. D is the outer diameter of the lining.

Considering the above factors, numerical models with load durations $t_d = 4$, 18, 110, and 184 ms, corresponding to the wavelength–diameter ratios $L/D = 1$, 5, 30, and 50, were established to examine the effects of the wavelength–diameter ratio on structural displacements, deformation change rules, and damage patterns.

3.2.1. Lining Displacement and Deformation. Figure 7 shows the time history curves of the vertical displacement of the same lining at different locations under different wavelengths of loading (t_d is the loading duration). In Figure 7(a), the vertical displacements of the top and the right side of the lining reach the peak at the end of the loading at that location, and the peak vertical displacement of the bottom node occurs at the end of the loading at that location for a period of time, and then, the vertical displacements of all the nodes gradually decrease. The rate of the decrease of the displacement of the top node is obviously larger than the rate of the decrease of the displacement of the right side and the bottom node. The peak vertical displacements at the top of the lining are significantly larger than those at the right and bottom, indicating that the vertical deformation of the structure mainly occurs in the upper part of the structure under the loading conditions where the wavelength is equal to the diameter of the structure. In Figure 7(b), the peaks of the vertical displacements at the top and right side of the lining occur before reaching the end of loading at that location, whereas the peak of the bottom vertical displacement is observed near the end of loading at that position. Subsequently, the vertical displacements of each node begin to gradually decrease with similar trends. In Figures 7(c) and 7(d), the displacement of

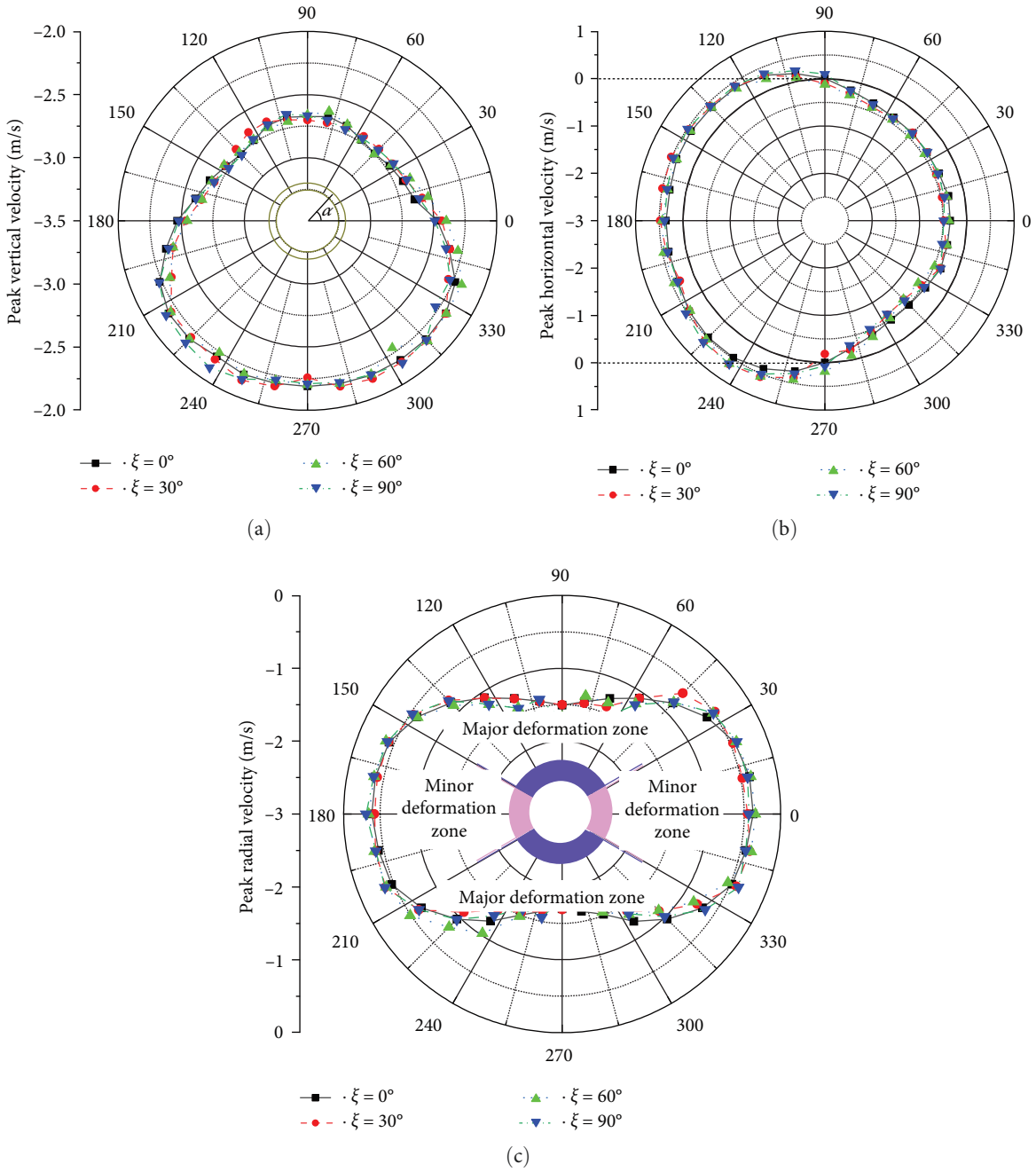

Figure 5: Peak velocity distribution with different incidence load angles: (a) peak vertical velocity, (b) peak horizontal velocity, and (c) peak radial velocity.

each node on the lining reaches its peak value before the load has ended at that position. Additionally, there is some variation in the displacement of each node on the structure during the loading process, suggesting both total displacement and structural deformation of the lining. At the end of the load, the vertical displacement curves of each node on the structure are largely identical, indicating that the structure is mainly a total displacement.

In Figure 8(a), the maximum horizontal displacement of the structure under load with the wavelength equal to the diameter occurs near the end time of the load, with some vibration after the displacement decreases to zero due to the interaction between the structure and the surrounding medium. Under all other conditions, the horizontal displacement reaches its maximum during the loading duration. In Figure 8(b), when the wavelength is 5 times the diameter of the structure, the horizontal displacement of the right side experiences a substantial change even after the loading action has ended. In Figures 8(c) and 8(d), for a wavelength that is 30 and 50 times the diameter of the structure, the right side's horizontal displacement shows a consistent pattern. It exhibits negligible vibration amplitudes during the loading phase and rests at nearly zero displacement

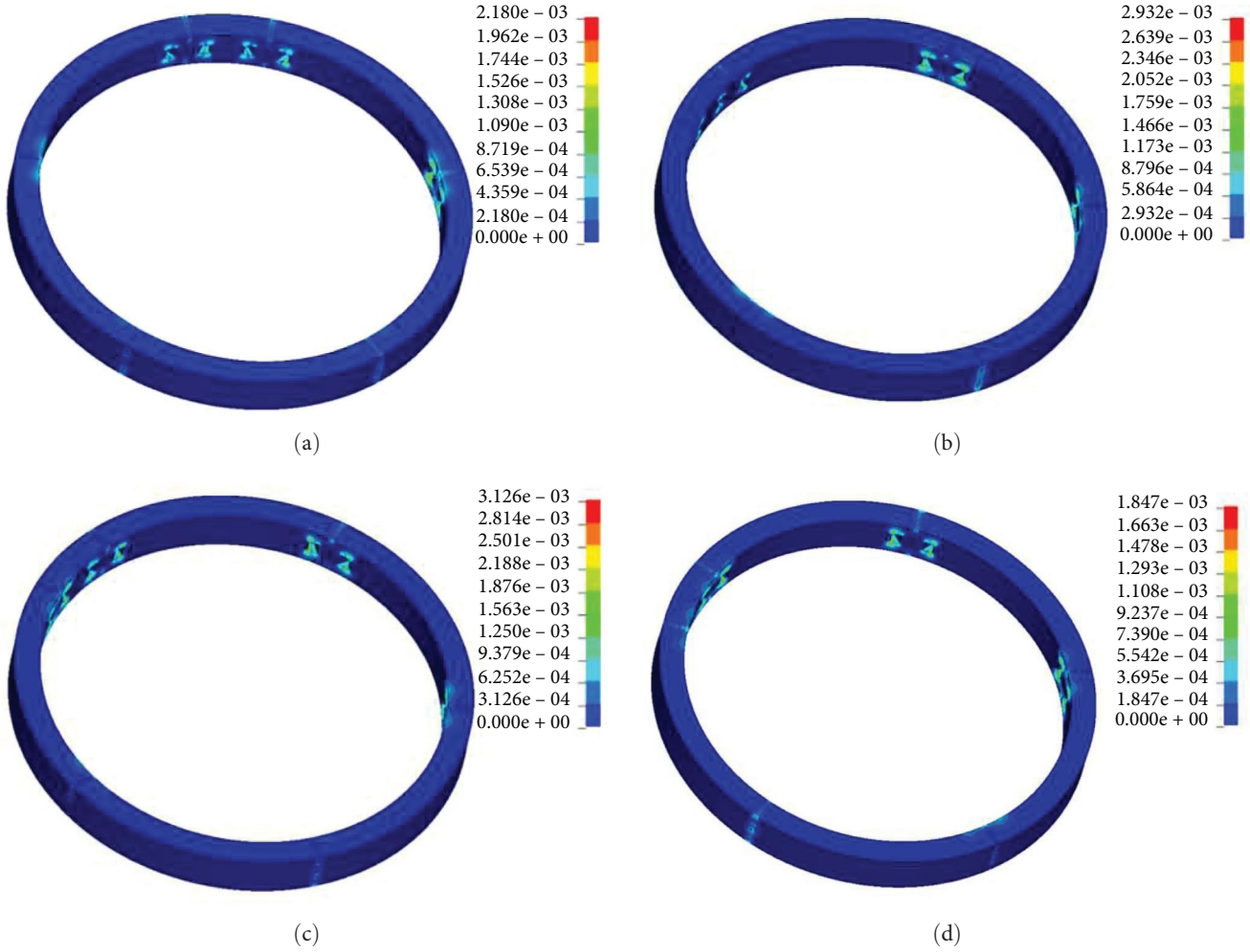

Figure 6: Distribution of plastic strain for different incidence load angles: (a) $\xi = 0°$, (b) $\xi = 30°$, (c) $\xi = 60°$, and (d) $\xi = 90°$.

Table 2: Maximum values of plastic strains for different incidence load angles.

ξ (°)	Position	Plastic strain ($10^3 \mu\varepsilon$)
0	Joint 6 ($\alpha = 11.25°$)	1.21
30	Joint 5 ($\alpha = 333.75°$)	2.93
60	Joint 5 ($\alpha = 3.25°$)	3.13
90	Joint 5 ($\alpha = 191.25°$)	0.82

at the loading's end, followed by a gradual increase and stabilisation.

A thorough examination of the displacement curves presented in Figures 7 and 8 reveals that, for identical structures, the vertical and horizontal displacements exhibit a longer response time than the duration of the applied load when the load wavelength is small. Furthermore, the displacement trends of the lining are largely similar for load wavelengths of 30 and 50 times the structure's diameter, with the displacement response time being approximately equal to the load duration. Under varying wavelengths of loading, the structure's response varies, with the exception of horizontal displacement at each node. As the loading wavelength increases, the peak displacement on the structure also increases.

Figure 9(a)–9(c) displays the peak vertical displacement, peak horizontal displacement, and peak radial displacement distribution of nodes on the lining in the annular direction during various wavelengths of loading, respectively. Since the difference between the peak vertical displacements of the lining under different wavelengths is large, the radial coordinates in Figure 9(a) are calculated as the dimensionless quantity in Formula (3), where $u_{y,\alpha,\max}$ is the peak vertical displacement of the node at the corner of α on the lining under specific conditions and $u_{y,\max}$ is the maximum value in $u_{y,\alpha,\max}$, and the specific values under different conditions are shown in Figure 9(a).

$$\overline{u}_{\alpha,\max} = \frac{u_{y,\alpha,\max}}{u_{y,\max}}. \tag{2}$$

In Figure 9, the peak vertical displacement of the node on the structure gradually increases with the loading wavelength increase, and the distribution law of the peak displacement

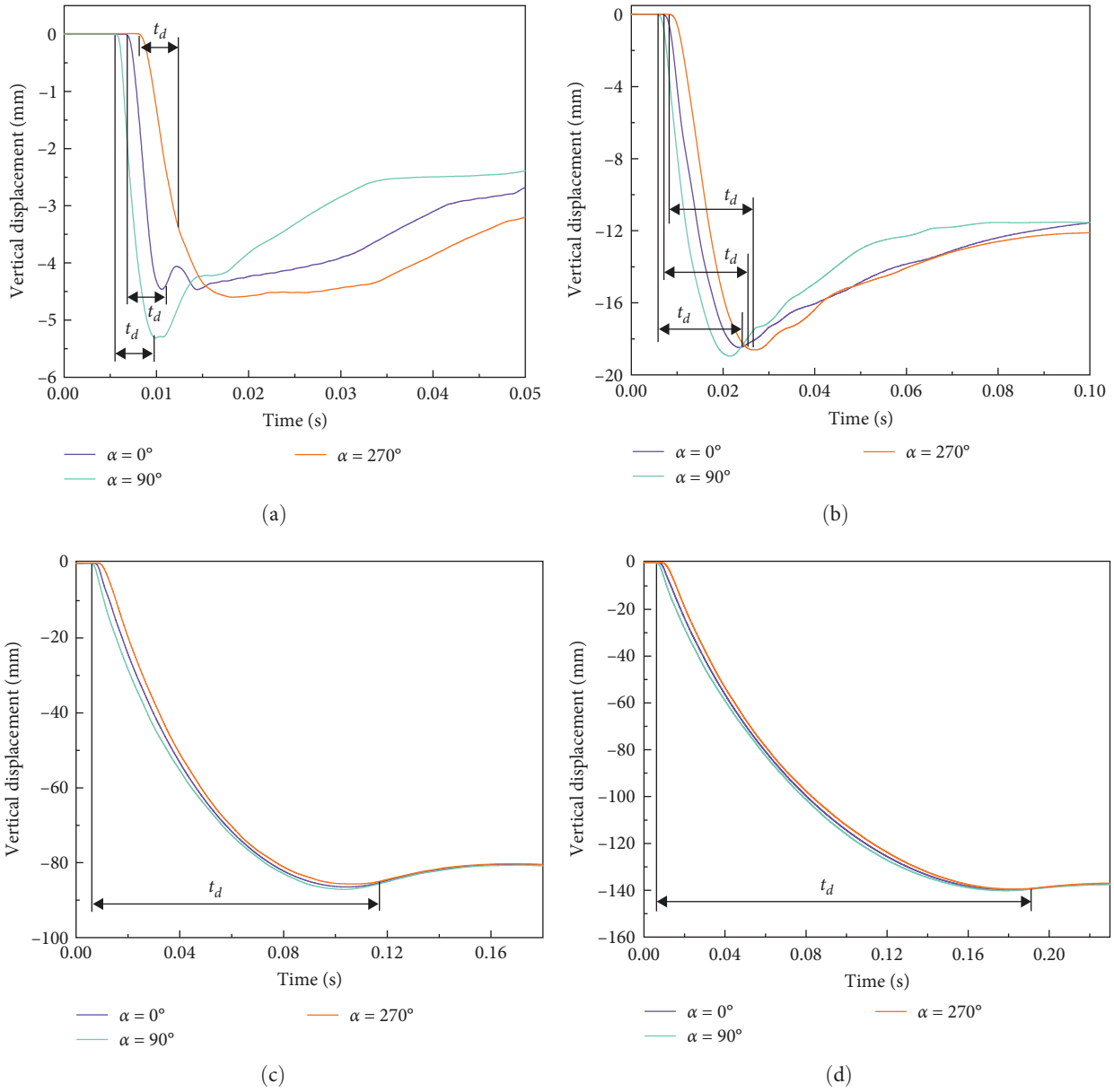

FIGURE 7: Vertical displacements with different wavelength–diameter ratios: (a) $L/D = 1$, (b) $L/D = 5$, (c) $L/D = 30$, and (d) $L/D = 50$.

undergoes some changes. When analysing the distribution of peak displacement curves under various wavelength-diameter ratios, we discovered that the vertical displacement occurs primarily within the angle range of $45° \leq \alpha \leq 135°$. With an increase in the wavelength–diameter ratio, the peak horizontal displacement of each node gradually increases, with its numerical magnitude and distribution law in the ring direction gradually converging. The peak radial displacement of the nodes increases gradually as the wavelength–diameter ratio increases. However, the change rule in the major deformation region and the minor deformation region differs slightly. In the major deformation region, the peak radial displacement of the nodes increases with the wavelength–diameter ratio at a rate inversely proportional to the wavelength–diameter ratio, and the peak displacement of $L/D = 5$ is significantly larger than that of $L/D = 1$. In the minor deformation region, the peak displacement of $L/D = 5$ is closer to the peak displacement of $L/D = 1$, whereas the peak displacement of $L/D = 30$ is slightly smaller than the peak displacement of $L/D = 50$.

The above analyses show that the peak radial displacement of the nodes in the major deformation region is more sensitive to the wavelength–diameter ratio when L/D is smaller ($1 \leq L/D \leq 5$), and when the wavelength exceeds a certain number of times of the structural diameter (the value is less than or equal to 30), the peak displacement is no longer changed with the increase of the wavelength–diameter ratio. The peak radial displacement in the minor deformation region is more sensitive to the wavelength–diameter ratio

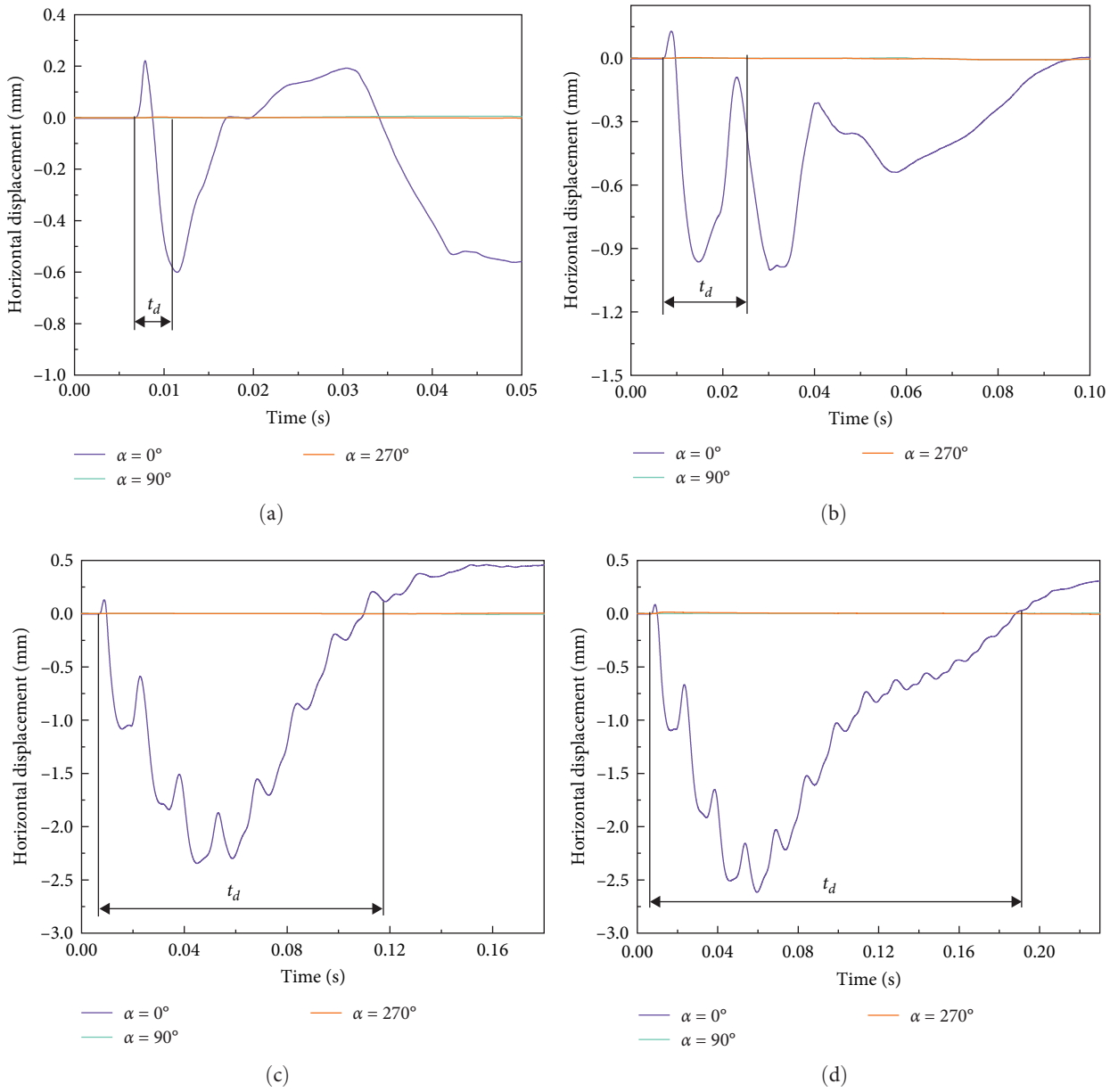

FIGURE 8: Horizontal displacements with different wavelength–diameter ratios: (a) $L/D = 1$, (b) $L/D = 5$, (c) $L/D = 30$, and (d) $L/D = 50$.

at $5 \leq L/D \leq 30$, and the peak radial displacement in the region remains basically unchanged at $L/D \geq 30$.

The above analyses indicate that there are structural deformation of the structure under the action of ground shock at different wavelengths, but the change characteristics of structural deformation in the time domain are missing. Since the longitudinal cross-section of the structure is circular, the degree of deformation of the structure can be described by the ellipticity ζ, which is calculated according to the following formula:

$$\zeta = 1 - \frac{R_2 + \Delta y}{R_2 + \Delta x}, \tag{3}$$

where Δx is the difference between the horizontal displacement of the right node and the left node of the lining and Δy is the difference between the vertical displacement of the bottom and top nodes of the lining.

Obviously, the closer ζ is to 0, the closer the structure is to a circle and the smaller the deformation is, and the closer ζ is to 1, the larger the deformation is. A positive value of ζ indicates that the structure is elongated horizontally and is in a "squashed" state, while a positive value of ζ indicates that the structure is elongated vertically and is in a "stretched" state. The deformation time of the structure is made dimensionless at $\overline{t} = (t - t_{as})/t_d$ (t_{as} is the time for the load to reach

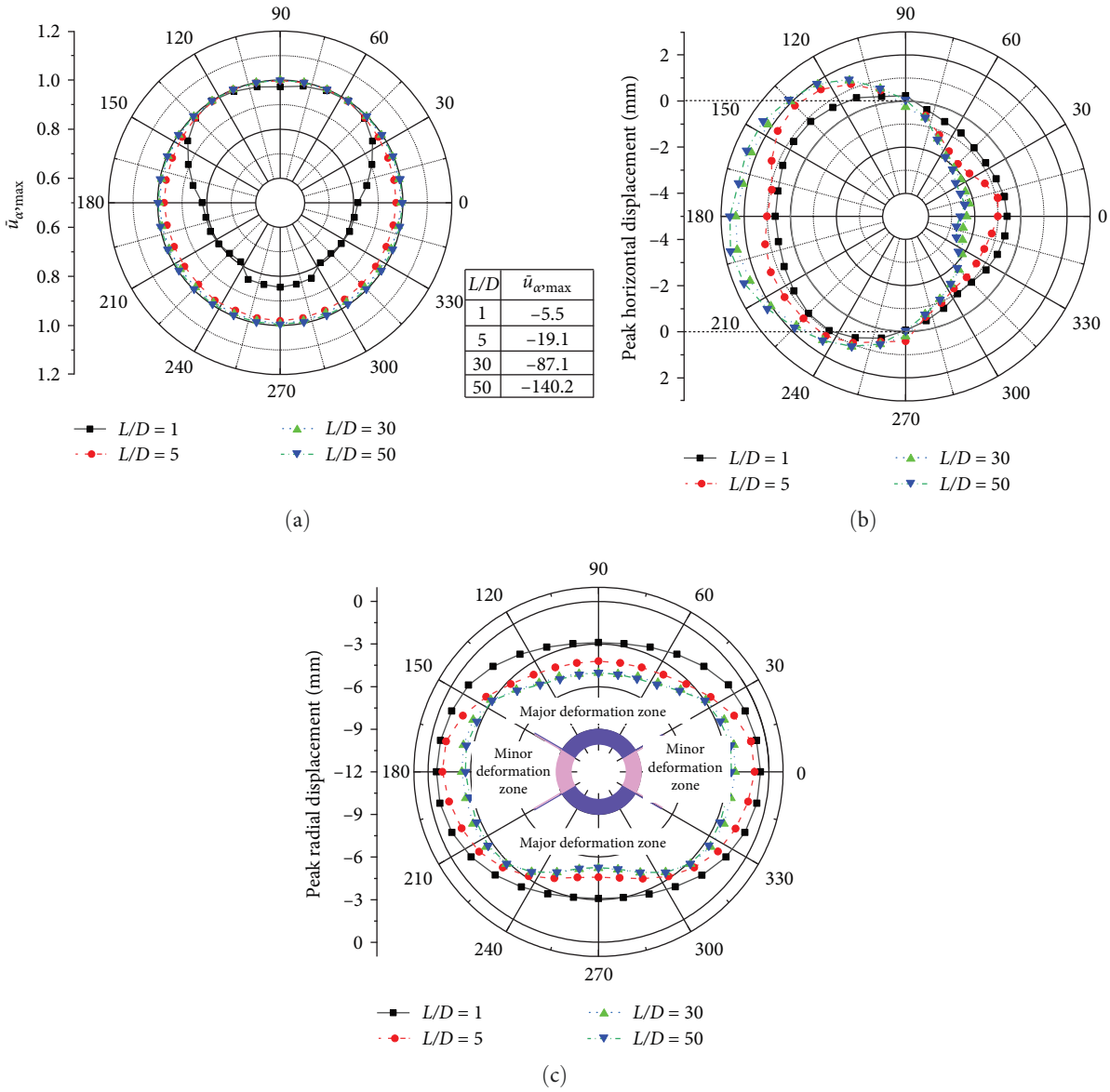

L/D	$\bar{u}_{\alpha,\max}$
1	−5.5
5	−19.1
30	−87.1
50	−140.2

Figure 9: Distribution of peak displacement for different wavelength–diameter ratios: (a) peak vertical displacement, (b) peak horizontal displacement, and (c) peak radial displacement.

the right of the structure), and the changes of structural ellipticity with $\bar{t}$ for wavelengths of 1, 5, 30, and 50 times the structural diameter are plotted in Figure 10.

Figure 10 illustrates that the response time for structural deformation is more than 3.5 times the duration of the load when the wavelength–diameter ratio is 1, with a maximum ellipticity of 0.17%. The duration of deformation response is around 2 times the load duration when the wavelength–diameter ratio is 5, with a maximum ellipticity of 0.34%. The duration of deformation response is approximately equal to the load duration when the wavelength–diameter ratios are 30 and 50, with maximum ellipticities of 0.395%. It is apparent that as the wavelength–diameter ratio increases, there is a tendency for the change in the rule of structural deformation over time to become consistent with the peak deformation. Furthermore, the structure is situated in a quasi-static load region [23].

3.2.2. Lining Velocity. From the above analysis, it can be seen that the structure under the ground shock mainly occurs in the vertical total displacement and a certain degree of structural deformation. Therefor, here we analyze the vertical velocity of the node on the lining under the ground shock with different wavelengths. The specific results are shown in Figure 11.

In Figure 11(a), the peak velocities of the top and right side of the lining manifest at the onset of loading, subsequently reducing swiftly, nearing zero velocities towards the end of loading, then rising in the opposite direction due to structural deformation and rebound, and finally converging to zero post a particular magnitude of vibration. The maximum speed of the bottom node is observed during the middle of the loading process and then slowly reduces to zero without any noteworthy vibration. In Figure 11(b), the velocity trend of each node over time is akin to that of $L/D = 1$ during the loading phase, followed by a minor

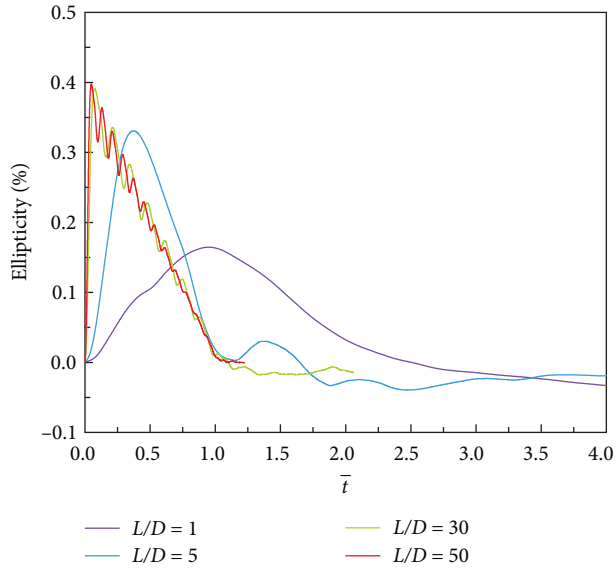

Figure 10: Ellipticity of lining for different wavelength–diameter ratios.

amplitude vibration at the end, and ultimately descending to zero. Moreover, the response time for vertical velocity is slightly greater than the loading duration. In Figures 11(c) and 11(d), the velocity of each node follows a similar pattern over time, reaching peak velocity at the start of the load action before gradually decreasing. The response time of the velocity of each node is consistent with the load duration, and the decline curve of the velocity of each node is also similar. This suggests that the structure of this stage is a total movement.

Figure 12(a)–12(c) shows the distribution of the peak vertical velocity, peak horizontal velocity, and peak radial velocity of the nodes in the annular direction of the lining for different wavelength–diameter ratios, respectively.

With the increase of the wavelength–diameter ratio, the trend of the peak vertical velocity of the nodes shows an increasing trend and the distribution curves in the annular direction tend to be consistent, and the distribution curves of the peak vertical displacements are basically the same for $L/D = 30$ and $L/D = 50$. In the major deformation region of the upper part of the structure and the minor deformation region on both sides, the distribution curves of $L/D = 5$ are closer to those of $L/D = 30$ and $L/D = 50$, while in the major deformation region of the lower part of the structure, the distribution curves of the peak vertical displacement of the structure of $L/D = 5$ differ greatly from those of $L/D = 1$ and $L/D = 30$, which indicates that the peak vertical velocity of the nodes in the major deformation region of the lower part of the structure is affected by the wavelength–diameter ratio more than that of the major deformation region.

The peak horizontal velocities of the nodes on the structure for varying wavelength–diameter ratios are consistent with the distribution law in the ring direction. The peak horizontal velocity resulting from the smaller wavelength is greater, and the peak horizontal displacement velocities of the nodes on the structure tend towards a certain value as the wavelength–diameter ratio increases.

As the wavelength–diameter ratio increases, the peak radial velocities of the nodes decrease gradually, ultimately converging. The nodes in the major deformation region of the upper part of the structure are more sensitive to the wavelength-diameter ratio, exhibiting a significant increase with the change of the wavelength–diameter ratio when $L/D \leq 30$. The upper and lower parts of the structure exhibit greater deformation velocities as the wavelength–diameter ratio varies. Based on Figure 9(c), the analysis indicates that the structure experiences greater deformation velocity when subjected to short wavelength loads, despite exhibiting smaller total displacement and deformation. These findings emphasise the importance of considering structural safety during the design process.

3.2.3. Lining Damage Characterisation. The plastic strain distributions of the structure subjected to ground shock with wavelength–diameter ratios of 1, 5, 30, and 50 are depicted in Figure 13(a)–13(d), respectively. It is apparent from the figures that the plastic strain region increases gradually on the structure with an increase in the wavelength–diameter ratio, all of which are concentrated at the segment joint. Moreover, the plastic strain distribution is nearly the same for $L/D = 30$ and $L/D = 50$. The preceding section examined the reason for the greater plastic strain at the handhole of the joint. The upcoming analysis will primarily focus on the size and distribution of plastic strain on the joint's surface.

Table 3 shows the maximum plastic strains on the structural joint surfaces and their locations of occurrence for the structure for different wavelength–diameter ratios. It can be found that the wavelength-diameter ratio does not affect the location of the maximum plastic strain on the structure. However, increasing the wavelength-diameter ratio will lead to an increase in the maximum plastic strain on the structure. This effect decreases with the increase of the wavelength–diameter ratio, and the maximum plastic strain is basically the same

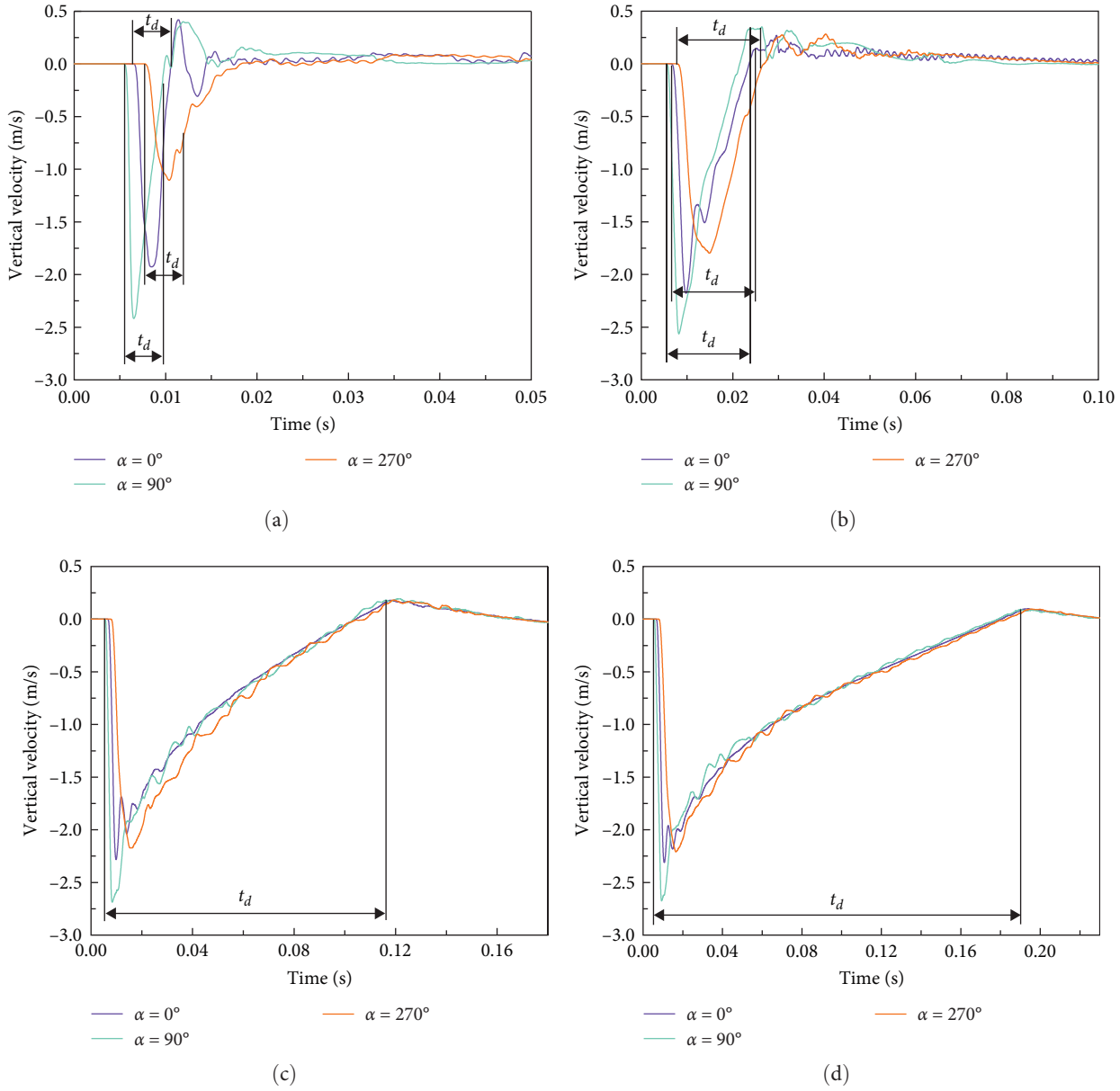

Figure 11: Vertical velocities for different wavelength–diameter ratios: (a) $L/D = 1$, (b) $L/D = 5$, (c) $L/D = 30$, and (d) $L/D = 50$.

when $L/D = 30$ and $L/D = 50$, which means that the structure is in a quasi-static load region under these conditions.

4. Conclusion

This paper presents a numerical model of the dynamic interaction between saturated soil and lining structure. The study analyses the effects of the incidence load angle and the wavelength-diameter ratio on the structural deformation pattern and damage characteristics. The conclusions drawn from the study are as follows:

(1) The structure shows a certain degree of vertical compression deformation under the ground shock, and according to the radial deformation of the structure, the structure can be divided into the major deformation region (the angle with the vertical direction is within 60°) and the minor deformation region (the angle with the horizontal direction is within 30°). The peak radial velocities of the nodes in the major deformation region are larger and faster, while the peak radial velocities of the nodes in the minor deformation region are smaller and basically equal in size.

(2) The plastic strain distribution pattern on the joint surface at the joint can be divided into two types. The first is concentrated near the outer surface and extends to the inner surface or even through the joint surface, and the second is concentrated near the inner surface and extends to the outer surface or even through the joint surface.

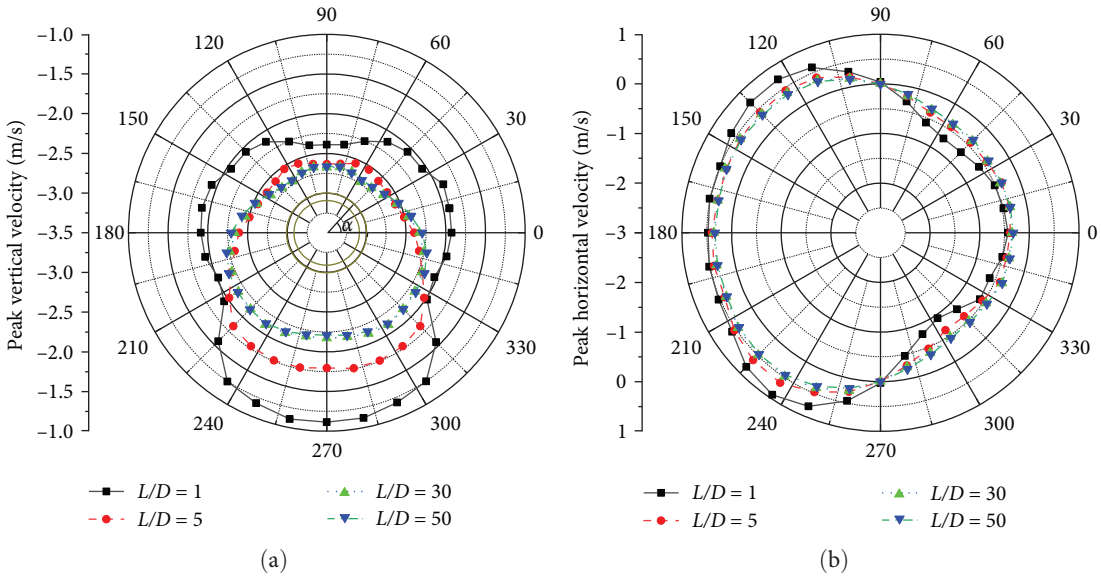

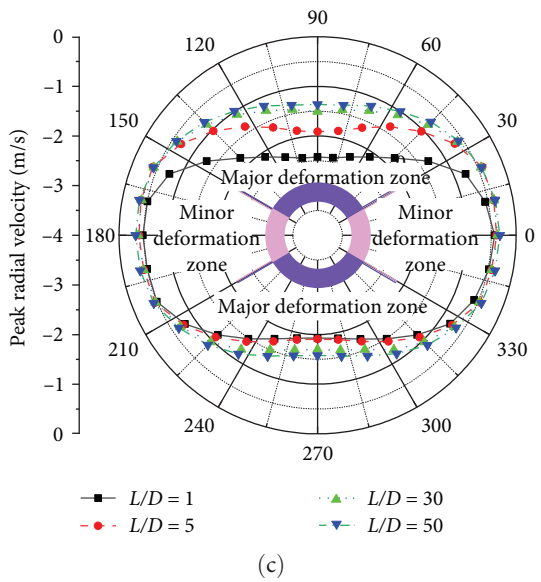

Figure 12: Peak velocity distribution for different wavelength–diameter ratios: (a) peak vertical velocity, (b) peak horizontal velocity, and (c) peak radial velocity.

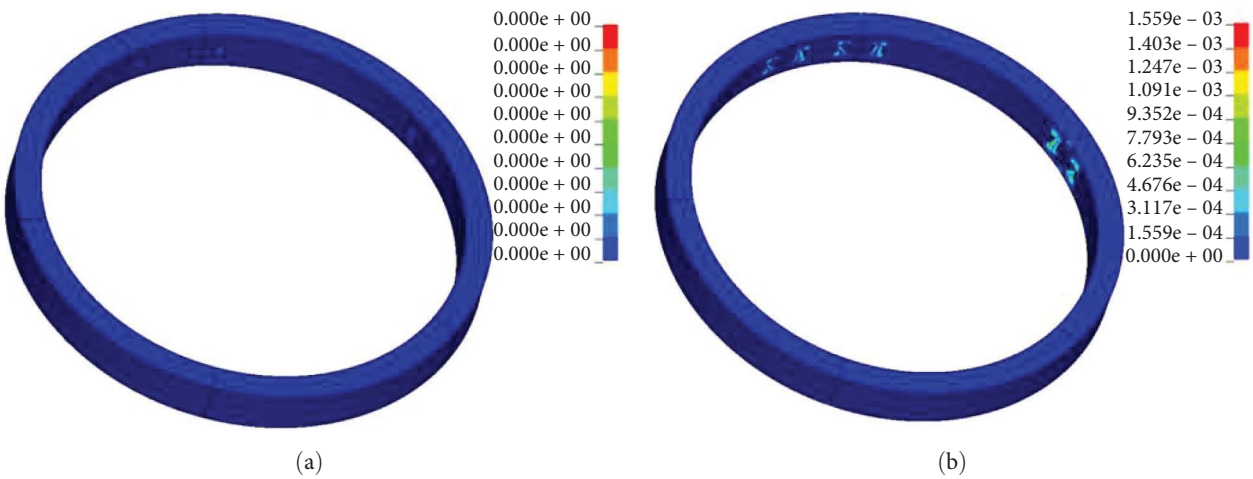

Figure 13: Continued.

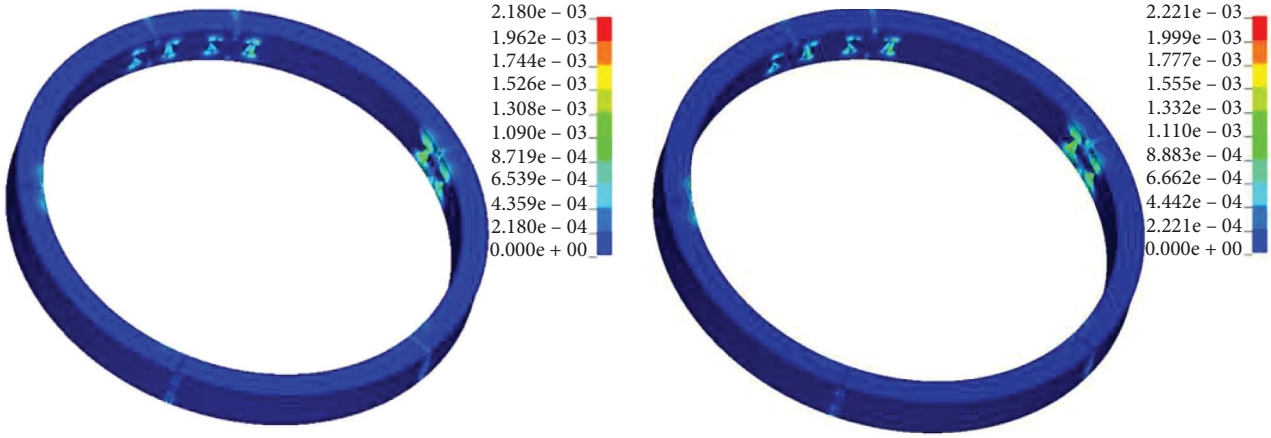

(c) (d)

Figure 13: Plastic strain distribution for different wavelength–diameter ratios: (a) $L/D = 1$, (b) $L/D = 5$, (c) $L/D = 30$, and (d) $L/D = 50$.

Table 3: Maximum values of plastic strains for different wavelength–diameter ratios.

L/D	Position	Plastic strain ($10^3\mu\varepsilon$)
1	Joint 6 ($\alpha = 11.25°$)	0
5	Joint 6 ($\alpha = 11.25°$)	0.45
30	Joint 6 ($\alpha = 11.25°$)	1.21
50	Joint 6 ($\alpha = 11.25°$)	1.24

(3) The incidence load angle basically does not affect the total displacement and velocity of the structure, but it will change the maximum deformation of the structure, the maximum velocity of the node, and the location of the maximum plastic strain. The plastic strain on the joint surface is the largest when the incidence load angle is 60°.

(4) As the wavelength–diameter ratio increases, the peak displacements and velocities in all directions of the nodes and the maximum plastic strain of the structure increase gradually. Additionally, the magnitude of the values and the distribution law in the annular direction gradually converge. The nodes in the major deformation region exhibit greater sensitivity to the wavelength–diameter ratio (L/D) when L/D is in the range of 1–5. Once the loading wavelength exceeds a certain number of times of the diameter of the structure, the peak displacements of the nodes are no longer changed with the increase of the wavelength–diameter ratio. The peak radial displacement in the minor deformation region is more sensitive to the wavelength–diameter ratio when L/D is in the range of 5–30. The peak radial displacement in the major deformation region and the minor deformation region remains basically unchanged when $L/D \geq 30$.

Data Availability

The data used to support the findings of this study are included within the article.

Conflicts of Interest

The authors declare that they have no conflicts of interest.

Acknowledgments

This study was financially supported by the Henan Provincial Department of Transportation, (2018J3), and the Henan Provincial Department of Education, (23A580005).

References

[1] Y. Zhao, C. Chu, and A. Vafeidis, "Vibration of a cylindrical tunnel under a centric point-source explosion," *Modelling of Structures under Seismic, Impact, and Shock Vibrations*, vol. 2017, Article ID 9152632, 7 pages, 2017.

[2] T. Namako, *MTA Terror-Proofs Bridges & Tunnels*, New York Post, New York, 2010.

[3] X. J. Guo, F. L. Min, X. C. Zhong, and W. Zhu, "Summaries of key technologies and difficulties in Nanjing yangtze river tunnel project," *Chinese Journal of Rock Mechanics and Engineering*, vol. 31, no. 10, pp. 2154–2160, 2012.

[4] K. Hong, "Analysis on technical difficulties of super-long underwater shield-bored tunnels with large cross-sections: case study on Shiziyang tunnel on Guangzhou-Shenzhen-Hong Kong passenger-dedicated railway," *Tunnel Construction*, vol. 6, pp. 1–3+18, 2007.

[5] H. Yuan, Q. H. Zhang, X. D. Hu, and P. Li, "Analysis of coupled anisotropic seepage and stress of large diameter river-crossing shield tunnel," *Chinese Journal of Rock Mechanics and Engineering*, vol. 10, pp. 2130–2137, 2008.

[6] M. Wang, "Current developments and technical issues of underwater traffic tunnel—discussion on construction scheme of Taiwan strait undersea railway tunnel," *Chinese Journal of Rock Mechanics and Engineering*, vol. 27, no. 11, pp. 2161–2172, 2008.

[7] S. Koneshwaran, D. P. Thambiratnam, and C. Gallage, "Response of segmented bored transit tunnels to surface blast," *Advances in Engineering Software*, vol. 89, pp. 77–89, 2015.

[8] Y. Yang, X. Xie, and R. Wang, "Numerical simulation of dynamic response of operating metro tunnel induced by ground explosion," *Journal of Rock Mechanics and Geotechnical Engineering*, vol. 2, no. 4, pp. 373–384, 2010.

[9] A. De, A. Niemiec, and T. F. Zimmie, "Physical and numerical modeling to study effects of an underwater explosion on a buried tunnel," *Journal of Geotechnical and Geoenvironmental Engineering*, vol. 143, no. 5, Article ID 04017002, 2017.

[10] A. Rashiddel, M. Kharghani, D. Dias, and M. Hajihassani, "Numerical study of the segmental tunnel lining behavior under a surface explosion—impact of the longitudinal joints shape," *Computers and Geotechnics*, vol. 128, Article ID 103822, 2020.

[11] P. Zhang, J. Cai, F. Zong, Y. He, and Q. Wang, "Dynamic response analysis of underground double-line tunnel under surface blasting," *Shock and Vibration*, vol. 2021, Article ID 9226615, 13 pages, 2021.

[12] L. Xiong, N. Jiang, C. Zhou, and H. Li, "Dynamic response characteristics of adjacent tunnel lining under blasting impact in subway connecting passage," *International Journal of Protective Structures*, vol. 14, no. 1, pp. 87–106, 2023.

[13] P.-C. Wang, L.-L. Sun, and Q.-Z. Kai, "Coupling thermo-hydro-elasto dynamic response of tunnel structure-saturated soil under thermo-mechanical shock," *Rock and Soil Mechanics*, vol. 33, no. 1, pp. 185–190, 2012.

[14] S. Wang, K. Wang, Y. Wang, Y. Liu, Z. Xu, and S. Liu, "Dynamic response analysis of segmental lining under ground shock: a simplified calculation method," *Advances in Civil Engineering*, vol. 2023, Article ID 8337511, 15 pages, 2023.

[15] S.-H. Wang, Y.-T. Zhao, Z.-H. Zhang, and S.-L. Liu, "Plane shock wave propagation in partially saturated soil," *Journal of King Saud University–Science*, vol. 34, no. 4, Article ID 101917, 2022.

[16] S. Liu, Y. Zhao, and S. Wang, "Method of vertical boundary setting for numerical model of structural dynamic response under yhe ground shock," *Protection Engineering*, vol. 44, no. 6, pp. 29–35, 2022.

[17] Z. Luo, *Theoretical Analysis and Experimental Research on the Resistance of Segmental Lining to Internal Explosion Action in Cross River Tunnel*, People's Liberation Army University of Science and Technology, Nanjing, 2012.

[18] J. O. Hallquist, "LS-DYNA keyword user's manual," *Livermore software Technology corporation*, vol. 970, pp. 299–800, 2007.

[19] S. Li, J. Zhang, and Z. Wang, "Simulation analysis of contact characteristics of the shield tunnel segment joints," *Journal of Liaoning University of Engineering and Technology (Natural Science)*, vol. 37, no. 6, pp. 899–904, 2018.

[20] Y. Liu, M.-Y. Wang, J. Li, D.-R. Wang, and N. Zhang, "Analysis of dynamic response of shield tunnel to explosion seismic wave," *Rock and Soil Mechanics*, vol. 35, no. 4, pp. 1056–1062+1068, 2014.

[21] B. Hao, *Underground Nuclear Explosions and Their Applications*, National Defence Industry Press, Beijing, 2002.

[22] C. Li and X. Li, "Influence of wavelength-to-tunnel-diameter ratio on dynamic response of underground tunnels subjected to blasting loads," *International Journal of Rock Mechanics and Mining Sciences*, vol. 112, pp. 323–338, 2018.

[23] T. Krauthammer, *Modern Protective Structures*, CRC Press, 2008.